Supplementary Information (SI) for ChemComm.

Supplementary Information

Tuneable Vacancy-Ordered Halide Perovskites Cs_2PdX_6 (X = Cl, Br) for Photoelectrochemical Water Splitting

Manasa Manoj,[ab] *Jigar Shaileshkumar Halpati,* [ab] *Aravind Kumar Chandiran* [ab*]

[a]*Department of Chemical Engineering, Indian Institute of Technology Madras, Adyar, Chennai, Tamil Nadu, India 600036.*

[b]*IITM-Hyundai Hydrogen Innovation Center, Indian Institute of Technology Madras, Adyar, Chennai, Tamil Nadu, India 600036.*

**aravindkumar@iitm.ac.in*

Experimental Methods

Synthesis of Cs_2PdCl_6

Cesium chloride (CsCl, Spectrochem, 99.5%) and palladium chloride ($PdCl_2$, Sigma Aldrich, 99%) are taken in 2:1 mol ratio and is added into a Teflon reactor followed by the addition of hydrochloric acid (HCl, Qualigens) and 10% (by volume) hydrogen peroxide (H_2O_2). It is then covered using a hydrothermal reactor and is kept in the oven at 120 °C for 6 hours. The obtained powder of Cs_2PdCl_6 is washed with ethanol a few times and the kept in hot air oven for drying at 70 °C for 12 hours.

Synthesis of Cs_2PdBr_6

Cesium bromide (CsBr, Alfa Aesar, 99.9%) and palladium bromide ($PdBr_2$, Sigma Aldrich, 99%) are taken in 2:1 mol ratio and is added into a Teflon reactor followed by the addition of hydrobromic acid (HBr, Rankem) and 10% (by volume) hydrogen peroxide (H_2O_2). It is then covered using a hydrothermal reactor and is kept in the oven at 120 °C for 6 hours. The obtained powder of Cs_2PdBr_6 is washed with ethanol a few times and the kept in hot air oven for drying at 70 °C for 12 hours.

Anion exchange

Cs_2PdCl_6 is transferred into 5 vials with 50 mg each which is then dispersed in a solution of 1M lithium bromide. After every minute, the powder in each vial is taken out, cleaned with ethanol and dried in hot air oven at 70 °C for 12 hours.

Material characterization

The powder X-ray diffraction pattern of the samples was measured using Thermo Fischer Scientific Equinox 3000 with Cu Kα as radiation source of wavelength 1.5406 Å. FTIR measurements were carried out using JASCO 6600FV spectrometer with an ATR setup. Measurements were taken from 4000- 50 cm^{-1} where the spectrometer was operated under complete vacuum for far-infrared measurements. Raman spectroscopic measurements were taken using confocal Raman spectrometer equipped with Nd:YAG laser of 532 nm excitation wavelength using WITec alpha 300 Confocal Raman System. High resolution images of the samples were taken using scanning electron microscopy (Hitachi S-4800) and the elemental composition and elemental mapping of the samples were obtained using Quanta 200 FEG energy dispersive X-ray spectroscopy. Absorption measurement of the samples was collected using Shimadzu UV-2600 UV−Vis−NIR spectrophotometer equipped with integrating sphere. Thermal decomposition of the samples was studied using SDT Q600, T.A. Instruments with the temperature ranging from room temperature to 900 °C at the ramp rate of 10 °C/min under nitrogen atmosphere.

pH stability: 50 mg of Cs_2PdX_6 (X= Br^-, Cl^-) powder was added to separate vials containing 3ml pH solution (pH 1, 5, 7, 11, 12, 13). pH solution is measured using using HI2215 pH/ORP meter (Hanna Instruments). This is kept undisturbed for 12 hours, washed with ethanol and finally dried in hot air oven at 70 °C. X-ray diffraction of the dried powder was carried out and compared with the as-synthesized material.

Photoelectrode preparation

FTO cleaning: FTO (Fluorine-doped tin oxide) glasses with area 1 x 2 cm^2 size were cut out from the 30 x 30 cm^2 FTO glass plate (Greatcell Solar, TEC7, 2.2 mm thickness). It is cleaned by ultrasonicating it in isopropyl alcohol (IPA), deionised water and fresh IPA (second time) for 20 min each. These FTOs are then heated at 500 °C for 1 h on hot plate.

Film formation: 15 mg of Cs_2PdX_6 (X = Cl^-, Br^-) was added to 200 µl isopropyl alcohol, 190 µl deionised water and 10 µl Nafion (5% w/w in water and 1-propanol). The solution is then ultrasonicated for 20 min. For electrochemical studies, 60 µl from the prepared solution is drop-casted onto the cleaned FTO and left undisturbed for drying under ambient atmosphere. An active area of 0.5 x 0.5 cm^2 is made by scrapping out the excess. For photoelectrochemical studies, cleaned FTOs are coated with compact TiO_2 layer using two-step procedure. Firstly, the cleaned FTOs are heated to 450 °C and a mixture of 1:39 ratio of titanium diisopropoxide bis(acetylacetonate) and ethanol is sprayed on the surface. Later the cooled FTOs undergo chemical bath deposition in which the FTOs are dipped in 40mM $TiCl_4$ solution and heated at 75 °C for 30 minutes in hot air oven. The bath is then taken out and poured with excess deionised water to remove the excess $TiCl_4$ in the solution. The substrates are then taken out and cleaned with deionised water and is heated on hot plate at 500 °C for 1 hour to form the layer of TiO_2. After cooling down, 60 µl of the prepared perovskite dispersion is drop casted on to the FTO with TiO_2 layer.

Electrochemical and photoelectrochemical characterization

All the electrochemical and photoelectrochemical studies are carried out using Versastat-3 electrochemical workstation with three electrode system. Ag/AgCl electrode filled with 3.5 M saturated KCl in DI water (17 MΩ resistance) is used as reference electrode and Pt coil as counter electrode. Cs_2PdX_6 coated on FTO is used as the working electrode. All the electrochemical experiments are performed with pH 11 solution as electrolyte prepared by adding required KOH to DI water and the pH is measured. In order to enhance the ionic conductivity of the electrolyte, 0.05M KCl is added as the supporting electrolyte.

Cyclic voltammetry: The measurements are performed at the scan rate of 0.02 V/s with the potential ranging from 0 V to 1 V to -1 V to 0 V.

Mott-Schottky: These experiments are performed to estimate the flat band potential of the samples. Measurements are taken at a fixed frequency of 100 Hz for the voltage ranging from 0 V to 0.5 V with an interval of 25 mV.

PEC measurements under light are conducted using a solar simulator (ScienceTech, Canada) that can simulate AM1.5G sun spectra. All the PEC measurements are done at 1 sun intensity.

Linear sweep voltammetry (LSV): It is measured under dark and light conditions at a scan rate of 0.02 V/s in the voltage range 0 V to 1 V. A home-made optical chopper controlled by an Arduino with ON/OFF timer is used for chopping measurement.

Electrochemical impedance Spectroscopy (EIS): EIS is carried out to measure the charge transfer resistance during the process in the frequency range from 1 MHz to 100 mHz where an AC voltage of 15 mV is applied along with the DC voltage which ranges from 0 V to 0.5 V with an interval of 0.1 V. EIS data is fitted using the equivalent circuit: $R_1 + Q_2/R_2 + Q_3/R_3$, where R_1 is the solution resistance, Q represents constant phase elements and R its corresponding resistance. Q/R indicate that both Q and R are connected parallelly.

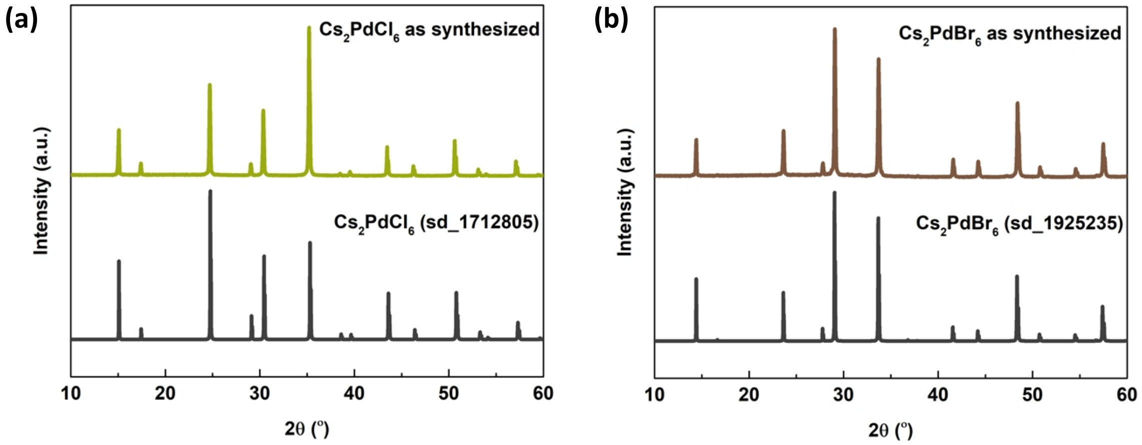

Figure S1. Comparison of X-ray diffraction patterns of as-synthesized material with database for **(a)** Cs_2PdCl_6 **(b)** Cs_2PdBr_6.[1,2]

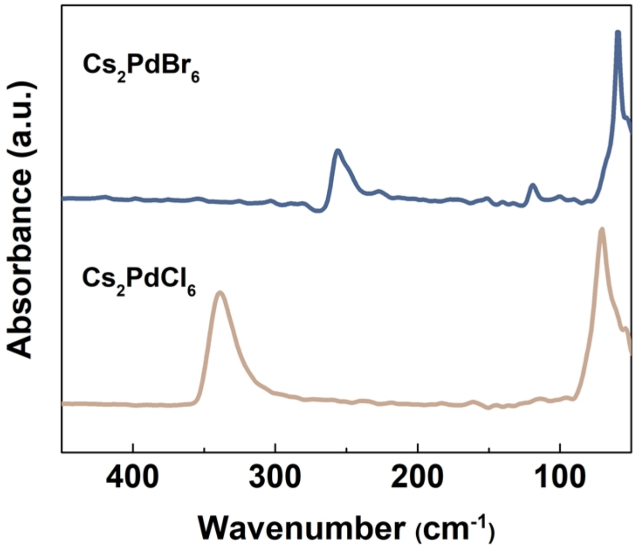

Figure S2. FT-far-IR spectra of Cs_2PdCl_6 and Cs_2PdBr_6

Fourier transform infrared (FTIR) spectroscopy was performed to analyze the materials (Figure S2). Cs_2PdCl_6 exhibited peaks at 338 cm^{-1} and 70 cm^{-1}, while Cs_2PdBr_6 showed peaks at 255 cm^{-1}, 118 cm^{-1}, and 59 cm^{-1}. The shift to lower wavenumbers in Cs_2PdBr_6 results from reduced vibrational frequency. The highest-frequency peak corresponds to Pd–X asymmetric stretching, while the lowest is due to Cs^+ ion rattling inside the octahedron.[3] Unlike Cs_2PdCl_6, Cs_2PdBr_6 displays an additional peak at 118 cm^{-1}, attributed to asymmetric Br–Pd–Br bending. Group theory predicts six vibrational modes, with IR activity dependent on dipole moment changes. The absence of an intermediate peak in Cs_2PdCl_6 suggests that Cl–Pd–Cl bonding does not significantly alter the dipole.

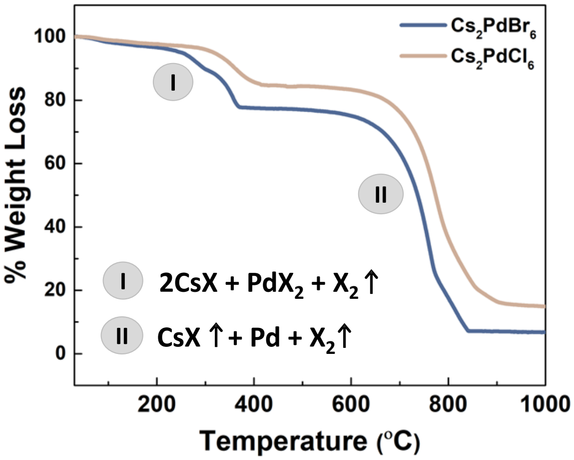

Figure S3. Thermogravimetric analysis of Cs_2PdX_6 (X = Cl^-, Br^-).

In the thermogravimetric analysis (TGA) of Cs_2PdCl_6 and Cs_2PdBr_6, a two-step decomposition pattern is observed, ultimately leading to the formation of elemental palladium as the final residue. The total weight loss measured corresponds closely with the theoretical mass loss expected if all other components (Cs and halides: Cl^- or Br^-) are volatilized or decomposed, leaving behind only metallic Pd. For instance, in the case of Cs_2PdCl_6, the theoretical Pd content based on its molar mass is approximately 18.2%, and the final residual mass observed in TGA matches this value, confirming that Pd is the sole stable phase remaining beyond 900 ^{o}C. A similar decomposition behavior is also observed for Cs_2PdBr_6, where the final residual mass of 12.5% remains indicating the presence of palladium. This behavior has been previously reported in literature by Ye et al. which discusses the two-step decomposition pathway of Cs_2PdBr_6, further validating the thermal decomposition mechanism.[4] After first step Cl_2 evaporates leaving behind $PdCl_2$ and 2CsX. Upon calculations, 87.8 % of the material remain. Upon further decomposition, CsCl and Cl_2 leaves the system leaving behind palladium and according to calculations, 18.2 % remains. A similar pattern is also followed by Cs_2PdBr_6 leaving behind approximately 80% and 18% after first and second decomposition, respectively. This theoretical calculation aligns with the TGA graph suggesting the validity of this two-step decomposition pathway.

(a) Cs_2PdBr_6 as synthesized

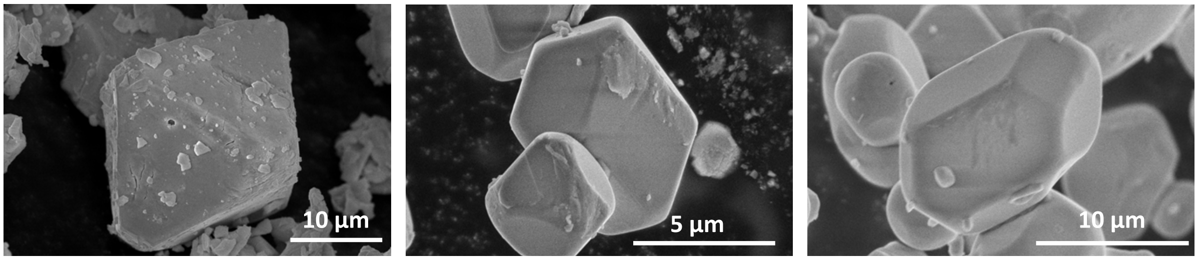

(b) Cs_2PdBr_6 after exchange

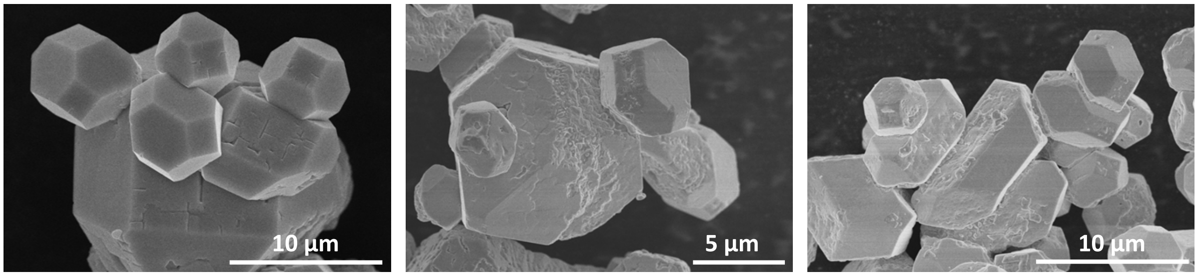

Figure S4. (a) SEM images of as synthesized Cs_2PdBr_6 (b) SEM images of anion exchanged e-Cs_2PdBr_6 from Cs_2PdCl_6 in LiBr solution

The particle size obtained through scanning electron microscopy (SEM) for Cs_2PdCl_6 and Cs_2PdBr_6 is observed to be in the range of 5–10 µm, and a similar particle size distribution is maintained by e-Cs_2PdBr_6 (Cs_2PdBr_6 obtained through anion exchange from Cs_2PdCl_6), as depicted in **Figure S4**. This suggests that the anion exchange process does not significantly alter the overall particle size of the material.

Additionally, the crystal structure of both the as-synthesized Cs_2PdBr_6 and the anion-exchanged e- Cs_2PdBr_6 appears to be similar, indicating that the structural integrity of the material is preserved during the exchange process. The retention of the particle size and crystalline morphology implies that the exchange occurs through a topotactic mechanism, wherein the anion substitution takes place without inducing significant changes in the particle size or disrupting the overall crystal framework.

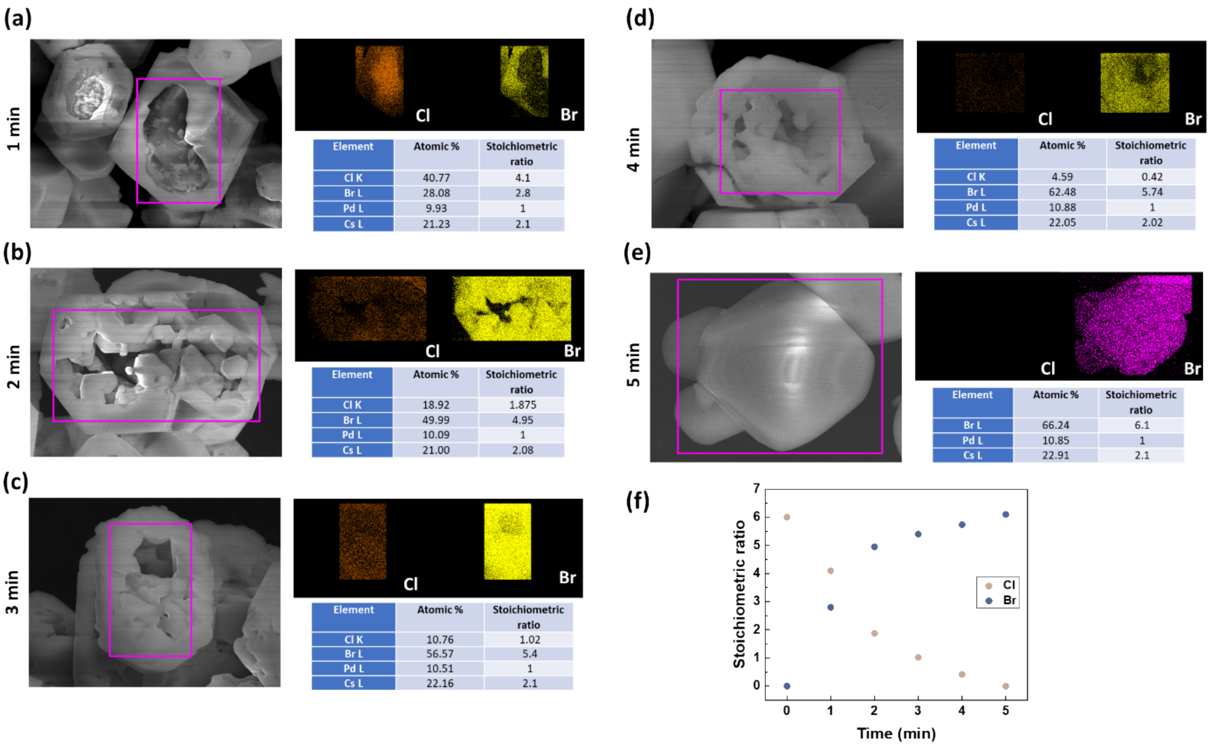

(a)

Element	Atomic %	Stoichiometric ratio
Cl K	40.77	4.1
Br L	28.08	2.8
Pd L	9.93	1
Cs L	21.23	2.1

(b)

Element	Atomic %	Stoichiometric ratio
Cl K	18.92	1.875
Br L	49.99	4.95
Pd L	10.09	1
Cs L	21.00	2.08

(c)

Element	Atomic %	Stoichiometric ratio
Cl K	10.76	1.02
Br L	56.57	5.4
Pd L	10.51	1
Cs L	22.16	2.1

(d)

Element	Atomic %	Stoichiometric ratio
Cl K	4.59	0.42
Br L	62.48	5.74
Pd L	10.88	1
Cs L	22.05	2.02

(e)

Element	Atomic %	Stoichiometric ratio
Br L	66.24	6.1
Pd L	10.85	1
Cs L	22.91	2.1

Figure S5. (a-e) Time dependent elemental mapping of the microcrystals at various time intervals during conversion **(f)** Stoichiometric ratio of chlorine and bromine in the material during anion exchange

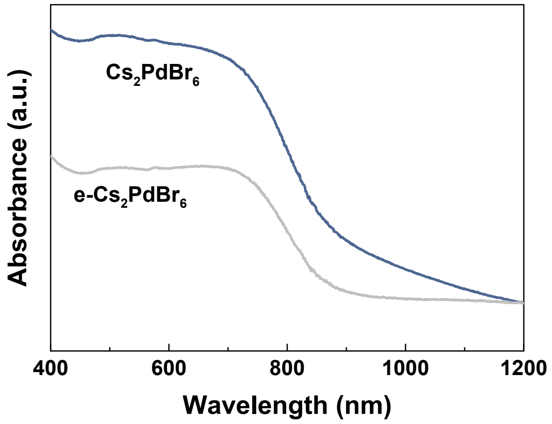

Figure S6. Absorption spectra of Cs_2PdBr_6 and e- Cs_2PdBr_6.

The strong absorption tail in the NIR region beyond 800 nm shall be attributed to the presence of halogen vacancies. The presence of vacancies is studied by comparing the absorption spectra of the as synthesized Cs_2PdBr_6 and e-Cs_2PdBr_6. As synthesized exhibited an absorption tail whereas e-Cs_2PdBr_6 did not exhibit any absorption tail beyond its onset. This can be due to the vacancies being filled by the bromide ions present in excess in the exchange medium.

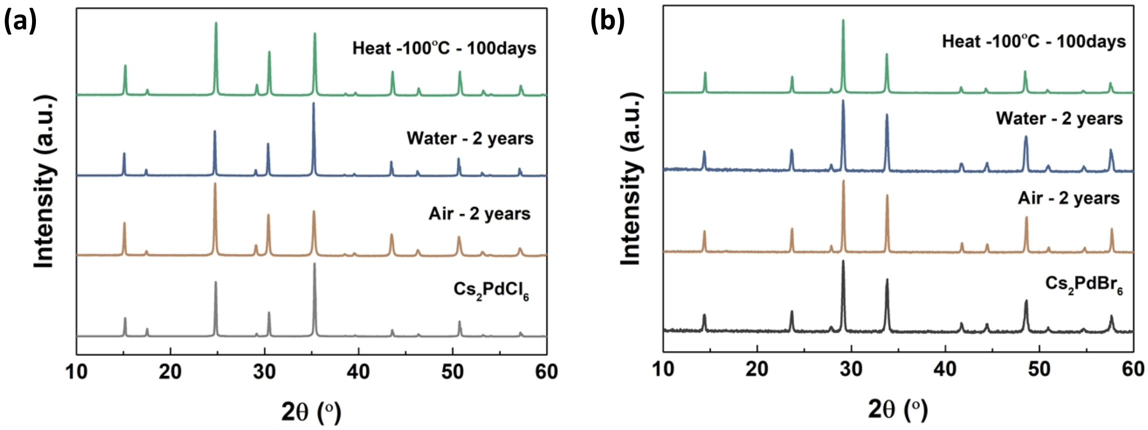

Figure S7. X-ray diffraction pattern of Cs_2PdX_6 (X = Cl, Br) after stability test under air, heat, and water

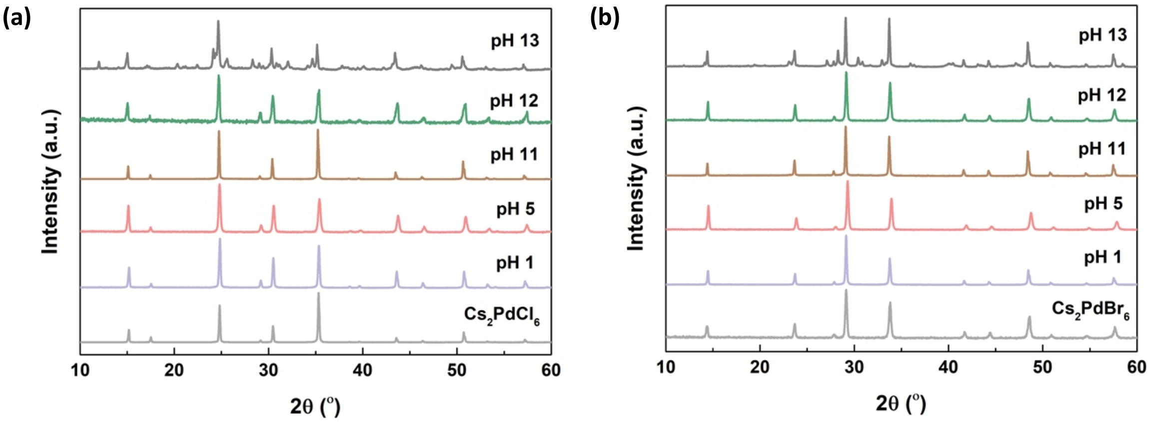

Figure S8. X-ray diffraction patterns of Cs_2PdX_6 (X = Cl, Br) after stability test at pH 1-13.

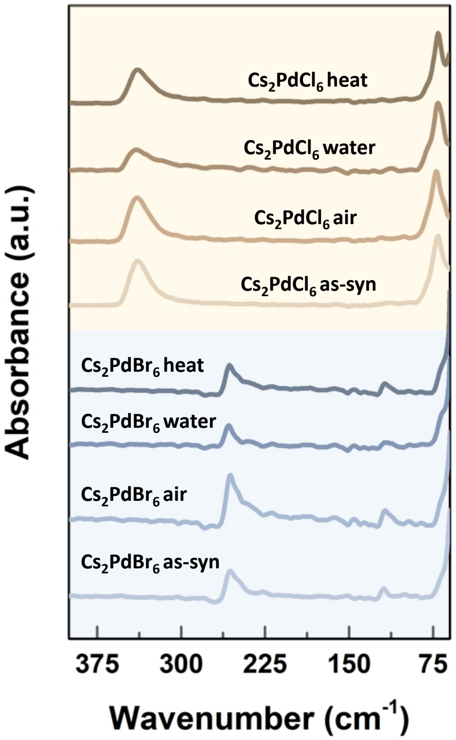

Figure S9. FTIR of Cs_2PdCl_6 (yellow region) and Cs_2PdBr_6 (blue region) after the stability tests

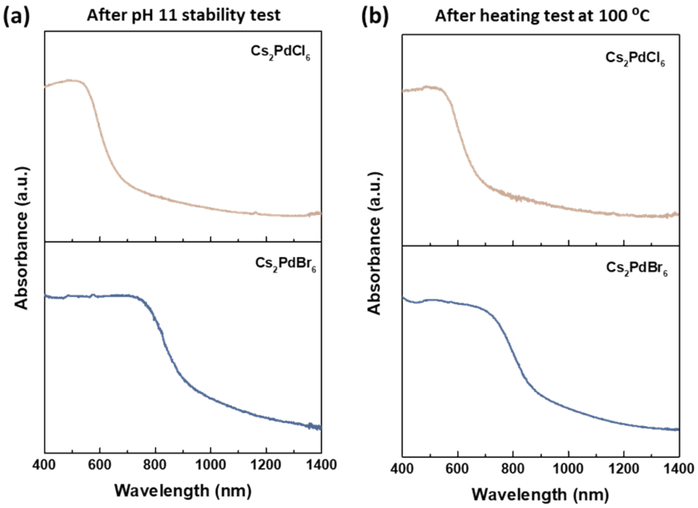

Figure S10. UV-Vis absorption spectra of Cs_2PdCl_6 and Cs_2PdBr_6 after **(a)** stability test in pH 11 **(b)** heat test

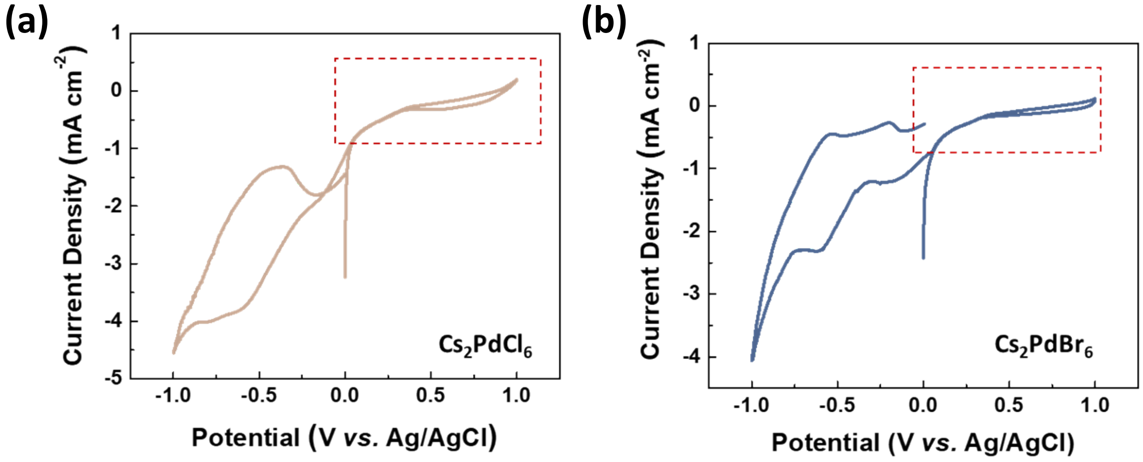

Figure S11. Cyclic voltammogram of (a) Cs_2PdCl_6 and (b) Cs_2PdBr_6.

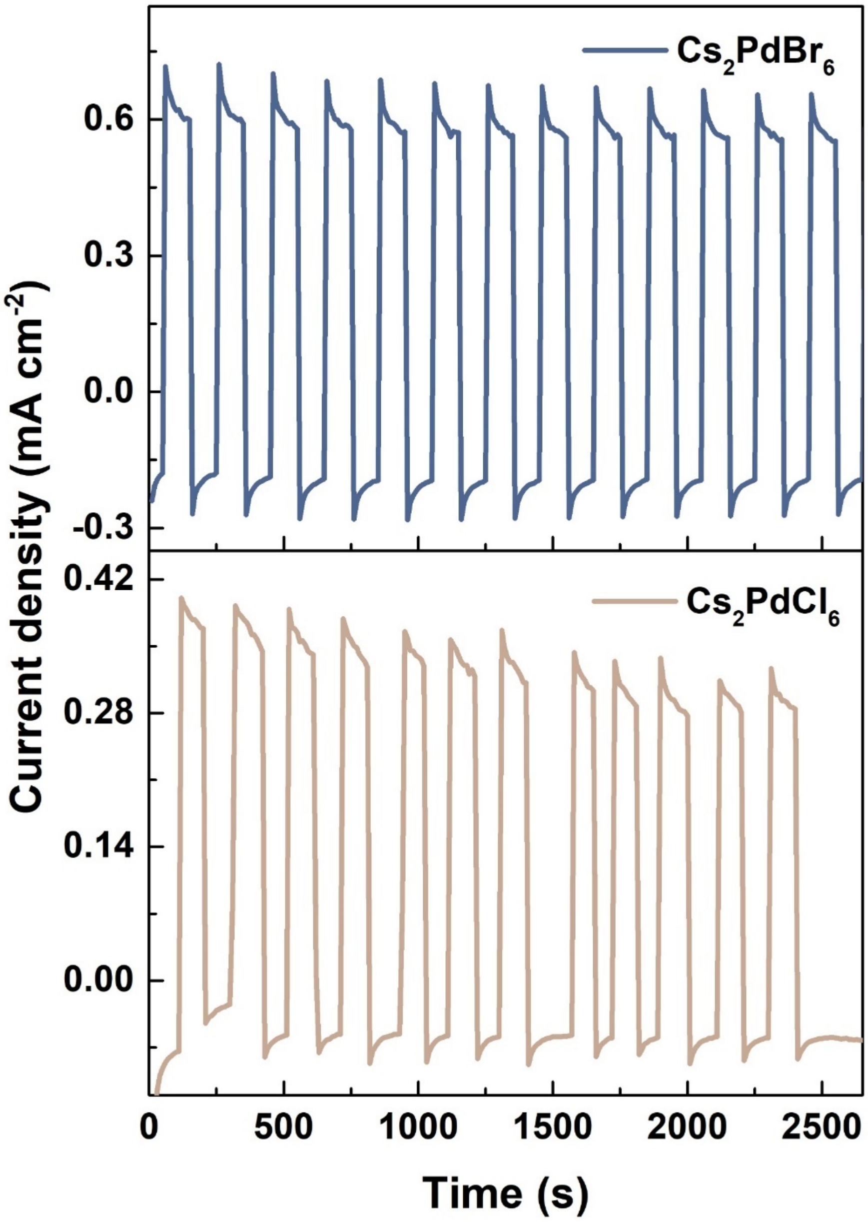

Figure S12. Chronoamperometry of Cs_2PdX_6 (X = Cl, Br).

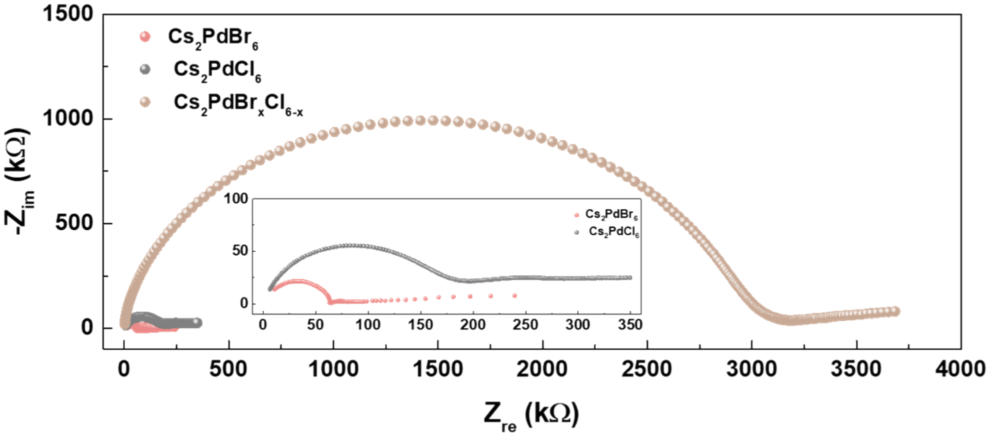

Figure S13. Comparative impedance spectra of Cs_2PdCl_6, Cs_2PdCl_6 and core-shell compounds.

Figure S14. Schematic of **(a)** core-shell particles as photoelectrode and **(b)** charge transfer pathways. Red lines represent ways through which transfer does not take place and black represents charge transfer pathway. This inhibition of charge transfer due to the presence of core reduces the number charge carriers available for reaction compared to the number of charge carriers generated. Dotted lines represent recombination pathways.

Table S1. Oxide materials, their vacancies and their corresponding bandgap.

S.No	Material	Vacancy	Bandgap Variation	Reference
1.	TiO_2	Oxygen	3.2 – 1.54 eV	[5–7]
2.	ZnO	Oxygen	3.37 – 3.05 eV	[8,9]
3.	SnTe	Tin	0.8 – 0.14 eV	[10]
4.	$SrSnO_3$	Oxygen	5.21 – 4.56 eV	[11]
5.	GaN	Gallium	3.2 – 3.15 eV	[12]

Explanation for the variation in the bandgap values:[13]

The choice of solvent combinations plays a crucial role in influencing nucleation rates, which, in turn, affect the crystallinity of the material. These variations in the crystallinity directly impact the absorption onset. In this work, a combination of hydrogen bromide (HBr) and hydrogen peroxide is utilized as the oxidation solution, followed by a longer reaction time under hydrothermal conditions. This approach is distinct from the methods reported in the existing literature.[13] Several studies have explored the tunability of the bandgap in halide perovskites by altering the deposition technique or the synthesis method. [14,15] For instance, a recent study on Cs_2TeBr_6 demonstrated bandgap tuning from 2.12 eV to 2.24 eV by modifying the solvent and precursor mixture.[16] The influence of solvent and precursor composition on the bandgap is a well-documented phenomenon in the literature. The presence of halide vacancies, as suggested from Figure S6, can significantly influence the electronic properties of materials. It is widely recognized that vacancies in the crystal structure tend to alter the bandgap of the material. This behaviour has been extensively reported in various oxide and semiconductor photocatalysts, where the introduction of vacancies can lead to changes in the material's optical and electronic properties.[17] A table of materials that exhibited a decrease in its bandgap due to an increase in the vacancies are as reported in Table S1.

References:

1 P. Villars and K. Cenzual, Cs2PdBr6 Crystal Structure: Datasheet from “PAULING FILE Multinaries Edition – 2022” in SpringerMaterials (https://materials.springer.com/isp/crystallographic/docs/sd_1925235) Springer-Verlag Berlin Heidelberg & Material Phases Data System (MPDS), Switzerland & National Institute for Materials Science (NIMS), Japan.

2 P. Villars and K. Cenzual, Cs2[PdCl6] (Cs2PdCl6) Crystal Structure: Datasheet from “PAULING FILE Multinaries Edition – 2022” in SpringerMaterials (https://materials.springer.com/isp/crystallographic/docs/sd_1712805) Springer-Verlag Berlin Heidelberg & Material Phases Data System (MPDS), Switzerland & National Institute for Materials Science (NIMS), Japan.

3 A. Kaltzoglou, M. Antoniadou, A. G. Kontos, C. C. Stoumpos, D. Perganti, E. Siranidi, V. Raptis, K. Trohidou, V. Psycharis, M. G. Kanatzidis and P. Falaras, *J. Phys. Chem. C*, 2016, **120**, 11777–11785.

4 W. Ye, Q. Cao, X.-F. Cheng, C. Yu, J.-H. He and J.-M. Lu, *J. Mater. Chem. A*, 2020, **8**, 17675–17682.

5 S. Guan, Y. Cheng, L. Hao, H. Yoshida, C. Tarashima, T. Zhan, T. Itoi, T. Qiu and Y. Lu, *Scientific Reports*, 2023, **13**, 14105.

6 Á. Balog, G. F. Samu, S. Pető and C. Janáky, *ACS Mater. Au*, 2021, **1**, 157–168.

7 J. A. Benavides-Guerrero, L. F. Gerlein, C. Trudeau, D. Banerjee, X. Guo and S. G. Cloutier, *Scientific Reports*, 2022, **12**, 15441.

8 J. Wang, Z. Wang, B. Huang, Y. Ma, Y. Liu, X. Qin, X. Zhang and Y. Dai, *ACS Appl. Mater. Interfaces*, 2012, **4**, 4024–4030.

9 S. A. Ansari, M. M. Khan, S. Kalathil, A. Nisar, J. Lee and M. H. Cho, *Nanoscale*, 2013, **5**, 9238–9246.

10 B. Kaur, R. Gupta, S. Dhiman, K. Kaur and C. Bera, *Pramana*, 2024, **98**, 149.

11 Q. Gao, H. Chen, K. Li and Q. Liu, *ACS Appl. Mater. Interfaces*, 2018, **10**, 27503–27509.

12 H. Ren, J. Jian, C. Chen, D. Pan, A. Ablat, Y. Sun, J. Li and R. Wu, *Applied Physics A*, 2014, **116**, 185–191.

13 N. Sakai, A. A. Haghighirad, M. R. Filip, P. K. Nayak, S. Nayak, A. Ramadan, Z. Wang, F. Giustino and H. J. Snaith, *J. Am. Chem. Soc.*, 2017, **139**, 6030–6033.

14 S. Fu, Y. Xiao, X. Yu, T. Xiang, F. Long, J. Xiao, Z. Ku, J. Zhong, W. Li, F. Huang, Y. Peng and Y. Cheng, *RSC Adv.*, 2021, **11**, 17595–17602.

15 S. A. Kulkarni, T. Baikie, P. P. Boix, N. Yantara, N. Mathews and S. Mhaisalkar, *J. Mater. Chem. A*, 2014, **2**, 9221–9225.

16 A. Brumberg, O. Kuklinski, G. T. Kent, E. E. Morgan, A. A. Mikhailovsky, T. A. Strom, M. L. Chabinyc and R. Seshadri, *Chem. Mater.*, 2024, **36**, 9625–9635.

17 B. Wang, J. Liu, S. Yao, F. Liu, Y. Li, J. He, Z. Lin, F. Huang, C. Liu and M. Wang, *J. Mater. Chem. A*, 2021, **9**, 17143–17172.